Applied Surface Science 586 (2022) 152827

Contents lists available at ScienceDirect

Applied Surface Science

journal homepage: www.elsevier.com/locate/apsusc

Full Length Article

Selective detection of sub-1-ppb level isoprene using Pd-coated In_2O_3 thin film integrated in portable gas chromatography

Hwaebong Jung [a,1], Hyegi Min [b,1], Junho Hwang [a], Jihee Kim [a], Yong-Sahm Choe [c], Hyun-Sook Lee [a,*], Wooyoung Lee [a,*]

[a] Department of Materials Science and Engineering, Yonsei University, 50 Yonseiro, Seodaemun-gu, Seoul 03722, Republic of Korea
[b] KIURI Institute, Yonsei University, 50 Yonseiro, Seodaemun-gu, Seoul 03722, Republic of Korea
[c] Isenlab Inc., Halla Sigma Valley, Dunchon-daero 545, Jungwon-gu, Seongnam-si, Gyeonggi-do 13215, Republic of Korea

ARTICLE INFO

Keywords:
Breath isoprene analyzer
Pd-coated In_2O_3 thin film
Metal catalyst
Gas chromatography
Selectivity

ABSTRACT

Monitoring breath isoprene concentration plays a role in non-invasive diagnosis of blood-cholesterol levels. In this study, we developed a highly sensitive and selective isoprene analyzer based on a Pd-coated In_2O_3 thin film integrated in a miniaturized gas chromatography column. To improve the sensing performance, the In_2O_3 thin films were fabricated with high uniformity and crystallinity using a dual-ion-beam sputtering system, and various metal catalysts (Au, Pt, and Pd) were loaded on the film surface. Among them, the Pd catalyst afforded the highest sensing reaction and the lowest detection limit (approximately 0.4 ppb), which is the best performance ever reported. It also significantly lowered the optimal operating temperature of the sensor from 432 °C to 196 °C. The excellent isoprene sensing performance of the Pd-coated In_2O_3 film can be attributed to the high density of oxygen vacancies, efficient reduction-reoxidation of PdO, and the Mars-van-Krevelen catalytic reaction. We further optimized the isoprene sensing performance of a Pd-coated In_2O_3 film by varying the Pd thickness and discovered that 1 nm of Pd deposition showed the optimal status of discontinuous islands for sensing. We expect that our device can be applied to a portable breath isoprene analyzer.

1. Introduction

Recently, exhaled breath analysis has gained great interest because it is a promising technology for noninvasive diagnosis of diseases. Human breath contains more than 250 kinds of endogenous volatile organic compounds (VOCs), which provide valuable information about physiological and pathophysiological conditions [1,2]. Isoprene is one of the most abundant exhaled VOCs [3], and its concentration in exhaled breath ranges from 22 to 234 ppb in healthy adults [4]. Isoprene is generated endogenously during metabolism, and an increase in breath isoprene concentrations has been linked to cholesterol biosynthesis [3], psychological stress [5], exercise [6], and many other conditions [7–9]. In particular, high blood cholesterol increases the risk of heart disease, which is a leading cause of death. Therefore, monitoring breath isoprene is important, and it can be a noninvasive diagnostic method to evaluate blood cholesterol levels or cholesterol synthesis rates [3].

Because the concentration of breath isoprene is excessively low, quantitative analysis of breath isoprene can be performed using high-performance equipment such as gas chromatography-mass spectrometry (GC–MS) [8,10], proton-transfer-reaction mass spectrometry (PTR-MS) [2,3,6], selected ion flow tube mass spectrometry (SIFT-MS) [7,9], laser spectrometry, and ion molecule reaction-mass spectrometry (IMR-MS) [11,12], all of which are commonly used in the laboratory. However, these techniques are expensive, limited in terms of portability, and require scientific personnel to operate. In order to overcome these problems, chemoresistive gas sensors based on metal-oxide semiconductors (MOS) have been studied extensively because the oxidation reaction on the MOS surfaces changes electrical resistance across the materials, which can be simply measured within short time with high sensitivity. In addition, they can be integrated into portable devices of compact size with low manufacturing cost [13]. Various MOS materials have been studied for the detection of isoprene, such as ZnO [14,15], TiO_2 [16], SnO_2 [17,18], and WO_3 [19]. Especially, lowest detection limit of isoprene (5 ppb) was observed at 325 °C for Ti-doped ZnO nanoparticles [14]. By combining Pt-doped SnO_2 nanoparticles with an active alumina filter, 500 ppb of isoprene could be selectively detected

* Corresponding authors.
E-mail addresses: h-slee@yonsei.ac.kr (H.-S. Lee), wooyoung@yonsei.ac.kr (W. Lee).
[1] These authors contributed equally.

https://doi.org/10.1016/j.apsusc.2022.152827
Received 26 July 2021; Received in revised form 23 January 2022; Accepted 10 February 2022
Available online 15 February 2022
0169-4332/

in a mixture of other gases such as ammonia, acetone, methanol, and ethanol [18].

In_2O_3, another well-known easily reducible MOS gas-sensing material, has been extensively studied for detecting various gases such as H_2, NO_2, H_2S, CO, CO_2, ammonia, acetone, formaldehyde, methane, and ethanol [20–27]. To the best of our knowledge, there is a paucity of reports on isoprene detection using In_2O_3 [28,29]. Recently, we reported the remarkable isoprene sensing performance of In_2O_3 nanoparticles [29]. It showed highest isoprene sensing response compared to that of reported so far and was able to detect the 1 ppb isoprene concentration at 350 °C. This result implies that In_2O_3 is a promising sensing material for use in high-sensitivity breath isoprene sensors. Even though they are integrated in the gas filter system to utilize a MOS-based gas sensor as a precise breath isoprene analyzer, there is a need to develop advanced sensors that can analyze the sub-ppb-level concentration. Several studies have reported that micro/nanostructure control, heteroatomic doping, and direct metal deposition on oxides are representative methods for enhancing gas-sensing performance by forming oxygen vacancies, tuning energy levels, and catalytic effects [30]. However, despite their outstanding sensing performance, there are still various obstacles such as the collapse of micro/nanostructures and unstable dopants in an oxide lattice at high operating temperature environment. The direct metal deposition method is one of the simplest ways to enhance the performance by inducing catalytic reaction even at harsh operating conditions, but the deposition does not uniformly cover the three-dimensional particles.

Compared to conventional approaches, we conclude that two-dimensional oxide thin films are good candidates because of their good crystallinity, high stability, and maximized catalytic effects [30]. In this approach, an In_2O_3 thin film was fabricated using dual ion beam sputtering (DIBS) as the deposition method and a noble metal was loaded as a catalyst. The DIBS method provides films with better compositional stoichiometry, uniform growth, and good adhesion to the substrate [31,32]. In addition, the loaded metal catalyst uniformly covers the entire surface of the oxide, enhancing the gas-sensing performance due to the increase in oxygen vacancies [30], spillover effects [33], and catalytic reactions of gas-phase molecule decomposition [34].

In this work, we report an excellent isoprene sensor based on a Pd-coated In_2O_3 thin film. For practical application as a portable breath-isoprene analyzer, the sensing performance of the In_2O_3 film sensor was tested by integrating it in miniaturized GC. Among the various catalysts of Au, Pt, and Pd, the Pd-coated thin film exhibited the best sensing performance, selectively detecting 0.4 ppb isoprene. Moreover, owing to the catalytic effect, the optimal working temperature could be significantly lowered from 432 °C for the pristine film to 196 °C for the Pd-coated film. By analyzing the surface states and elemental distributions, we revealed that the superior sensing performance of Pd-coated sensor was due to the larger amounts of deficient oxygen [30], efficient reduction-reoxidation transition [34], and Mars-van-Krevelen catalytic reaction [35–38].

2. Materials and methods

2.1. Synthesis of catalyst-coated In_2O_3 thin films

The In_2O_3 thin films were deposited on an Al_2O_3 substrate (5 × 2.5 mm^2) using a DIBS system (Fig. 1(a)). Before the deposition of the thin films, interdigitated electrodes (Pt, 100 nm in thickness) and heaters (Pt, 600 nm in thickness) were fabricated on the top and bottom surfaces of the alumina substrates, respectively, using a DC sputtering system. The patterned alumina substrates were loaded onto the sample holder of the DIBS system. Here, two distinct ion sources were used: a primary ion source was used to sputter an indium oxide target (99.99%) under an Ar gas flow condition at a rate of 34 sccm. Then, a secondary ion source was simultaneously used to compensate for the low oxygen composition by controlling the flow rate of the oxygen ions (34 sccm). Therefore, the thin films deposited using this technique exhibit exact stoichiometry [39]. During the sputtering process, the base pressure was approximately 1×10^{-5} Torr. Acceleration voltage and current density were adjusted to 1.0 keV and 1.5 $mAcm^{-2}$, respectively, for the primary ion source, and 200 eV and 0.2 $mAcm^{-2}$, respectively, for the secondary ion source.

After DIBS, the deposited In-O alloy films were annealed at 500 °C for 5 h in an ambient air atmosphere in an electrical furnace to form a crystalline In_2O_3 thin film (Fig. 1(b)). After annealing, Au, Pt, or Pd were deposited on the surface of the heat-treated In_2O_3 thin films using a power of 20 W (Pt and Pd) or 30 W (Au) in an Ar atmosphere. The deposition rates of Au, Pt, and Pd were 0.67 nm/s, 0.28 nm/s, and 0.31 nm/s, respectively. Thereafter, the thicknesses of the catalysts were adjusted to 1 nm by controlling the deposition time. To load the metal catalyst using an ultra-high vacuum DC magnetron sputtering system, high-purity catalyst targets (4 N) were used. The base pressure was approximately 4×10^{-8} Torr, and the deposition process was conducted at an Ar flow rate of 34 sccm under a pressure of less than 2.3×10^{-3} Torr.

2.2. Characterization of catalyst-coated In_2O_3 thin films

The detailed crystal structures of the as-synthesized In_2O_3 thin films were investigated by X-ray diffractometer (XRD, SmartLab, Rigaku) using Cu Kα radiation and transmission electron microscopy (TEM, JEOL JEM-F200). The overall surface morphology and uniformity of the as-prepared films were analyzed using scanning electron microscopy (SEM, JEOL-7610F-Plus, JEOL Ltd.) images and X-ray reflectometry (XRR, SmartLab, Rigaku). The roughness and surface area of the samples were analyzed by an atomic force microscope (AFM, Dimension ICON, Bruker Nano Surface). For the TEM analysis, the thin films were cut perpendicular to the top surface using a focused ion beam system (FIB, Crossbeam 540, ZEISS), and the cross-sectional surface of the film was investigated. Surface elemental analysis was conducted by X-ray photoelectron spectroscopy (XPS, K-alpha Thermo U. K.) using Al *Kα* radiation. The elemental dispersion of the catalysts on the surface of the In_2O_3 thin films was examined using field-emission scanning electron microscopy (FE-SEM, JEOL-7001F, JEOL Ltd.) equipped with an energy-dispersive X-ray spectroscope (EDS). To quantitative analysis, the In_2O_3 thin films were deposited on a silicon substrate and totally digested in the 2 : 3 : 5 mixture of HNO_3, HCl, and HF (aqua regia) followed by being analyzed using an inductively coupled plasma-optical emission spectrometry (ICP-OES, OPTIMA 8300, PerkinElmer).

2.3. Evaluation of isoprene sensing performance

The isoprene sensing performance of the In_2O_3 thin films with and without metal coating was evaluated using a mini- GC (Fig. 2). The instrumental details have been described in detail in a previous study [40]. In brief, the device had dimensions of 8 × 13 × 16 cm^3 and consisted of a sampling loop (1 ml), a packed column, three solenoid valves, a mini-sized pump, and a sensor based on In_2O_3 thin film. The volume of the isoprene sampling gas was limited to 1 ml and dry air with a flow rate of 20 sccm was used as the carrier gas.

The sensing process of the manufactured mini-GC was as follows (see Fig. 2): 1 ml of air and target gas mixture was filled into the sampling loop for 10 s without pre-concentration. Then, the gas mixture was injected into the packed column, and the components of the gas were separated by different strengths of interaction between the gas molecules and the stationary phase. The stationary phase coated on the column filler had a weak polarity. Therefore, non-polar gases (e.g., N_2 and CO_2) and smaller gas molecules are released from the column faster than the others. The separated gas components were passed through the packed column by a constant flow of the carrier gas (dry synthetic air). The temperature of the column during the operation was maintained at 30 °C. The target gas that passed through the column was detected using

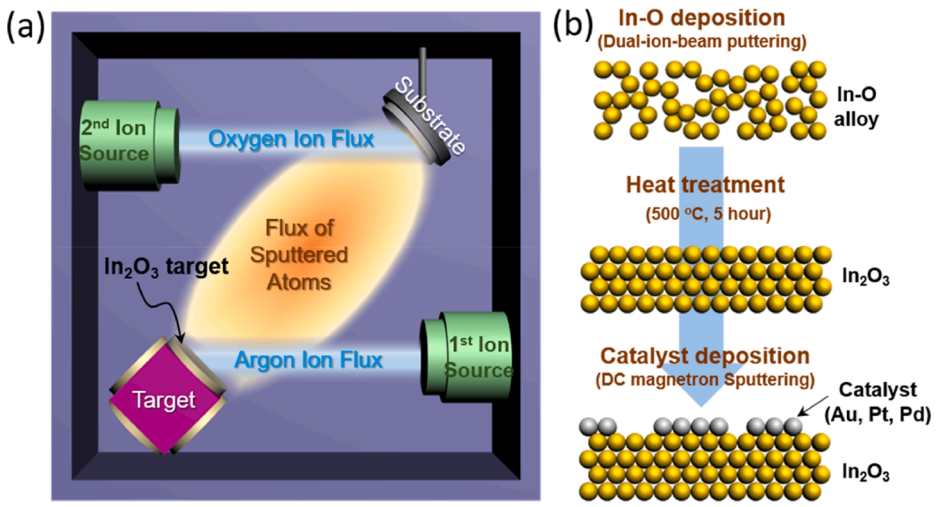

Fig. 1. (a) Schematic of the dual-ion-beam sputtering system used to deposit In-O alloy; (b) Schematic of the synthesis procedure of catalyst-coated In_2O_3 thin films.

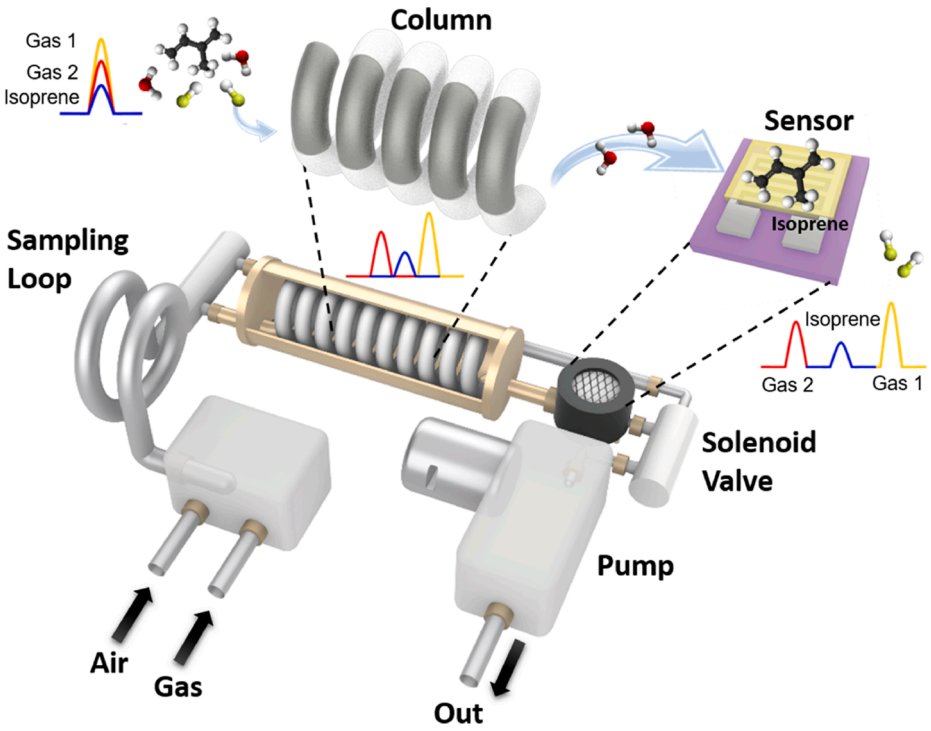

Fig. 2. Schematic of the interior components and selective detection mechanism of the mini-GC device integrated with catalyst-coated In_2O_3 thin film sensors.

as-prepared In_2O_3 thin films. To detect isoprene with high sensitivity and selectivity, the length and inner diameter of the packing column (Isenlab, Inc.) were adjusted to 90 cm and 0.4 cm, respectively. To optimize the operating temperature of the isoprene analyzer, the response of the device was tested over a wide range of 156–452 °C. The ability of the analyzer to sensitively detect isoprene was investigated at various concentrations of isoprene in the range of 0.0004 ppm - 25 ppm at the optimal working temperature.

The sensing performance was evaluated based on a sensor signal converted from the logarithm of the sensor resistance (log(R)), which was obtained using a gas analyzer. The sensing response of the samples was defined as the Δ sensor signal, which is the peak height of the sensor signal [40]:

$$\Delta \text{ Sensor signal} = \Delta \log(R) = \log(R_{air}) - \log(R_{gas}) = \log(R_{air}/R_{gas}), \quad (1)$$

where $\log(R_{air})$ and $\log(R_{gas})$ are the maximum values before and after exposure to isoprene, respectively.

3. Results and discussion

To investigate the nanostructure of the metal-coated In_2O_3 thin films, we carried out TEM analysis. On the cross-sectional surface of the Au-coated In_2O_3 thin film, we readily found a stack of Al_2O_3 substrate, In_2O_3 thin film, and Au-catalyst layer (Fig. 3(a)). On the top surface, the Pt layer is a protective layer for the FIB specimen preparation. As expected, the DIBS process resulted in a highly crystalline In_2O_3 thin film with a thickness of ~ 40 nm over a large area (Fig. 3(a)). As can be seen in the high-resolution TEM image in Fig. 3(c), the interplanar distance was approximately 0.292 nm, which corresponds to the *d*-spacing of the (222) planes of cubic In_2O_3. For metal loading, we adjusted the

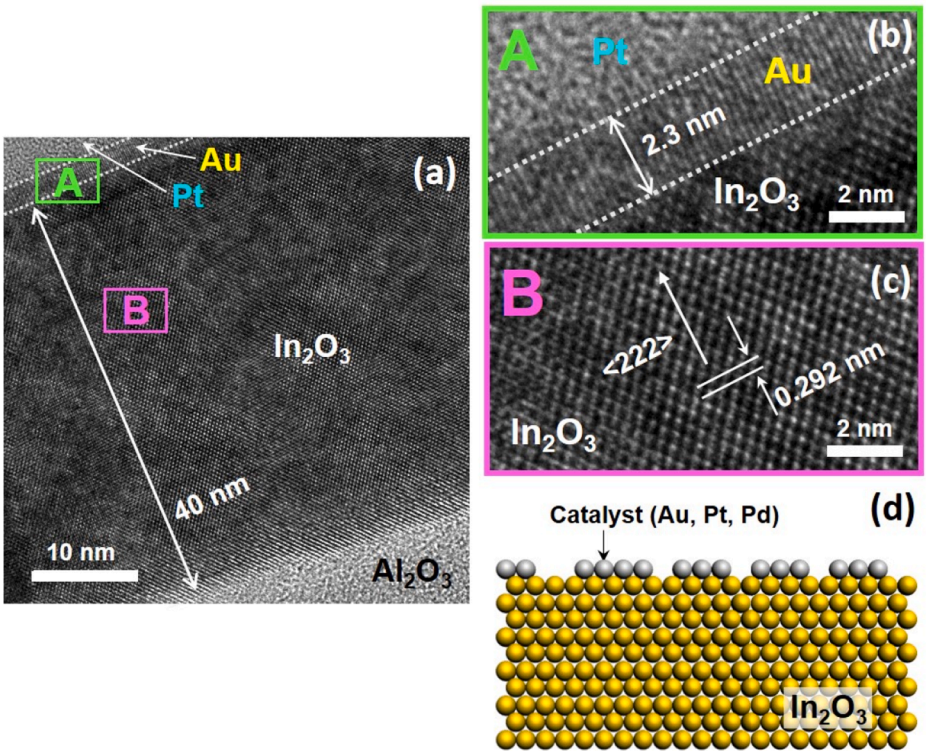

Fig. 3. (a) TEM image of the cross-sectional surface of the Au-coated In_2O_3 thin film; (b) and (c) High-resolution TEM images obtained from the areas marked A and B in (a); (d) Schematic diagram of the catalyst-coated In_2O_3 thin film.

deposition time to obtain an 1 nm thick catalytic layer. However, the TEM image shows that the thickness of the Au layer was approximately 2.3 nm (Fig. 3(b)), indicating locally distributed discontinuous islands rather than a uniform and widely dispersed thin layer (Fig. 3(d)). This catalyst layer could be easily distinguished from the Pt and In_2O_3 layers because of its distinctive atomic structure.

To analyze the overall surface morphology and uniformity of the as-prepared In_2O_3 thin films, we obtained SEM images and XRR patterns. For the measurements, we prepared pristine In_2O_3 thin film, metal-coated In_2O_3 thin films with different metals (1 nm Au, Pt, and Pd deposition), and Pd-coated In_2O_3 thin films with different Pd thicknesses (3 and 5 nm deposition) on SiO_2 substrates (10×10 mm^2). According to low magnification SEM images (Fig. S1), the pristine In_2O_3 films were uniformly formed on the substrate over the 1 cm^2 area through the DIBS and heat treatment. At high magnification over 10 k (Fig. S1), we could see stacked small crystalline structures formed after heat treatment of amorphous In-O alloys at 500 ℃. Fig. S2 shows the surface morphologies of the metal catalysts (Au, Pt, and Pd) deposited on the In_2O_3 film surface. The surface morphology of the In_2O_3 films is found to be dependent on a type of metal catalyst. While Au formed large islands of irregular shapes (Fig. S2(a)), which is in good agreement with the TEM image. (Fig. 3), the Pt-coated surface turns out to be similar that of pristine In_2O_3 thin films (Fig. S2(b)). Moreover, Pd was deposited in small island patterns with nanogap grain boundaries (Fig. S2(c)). The different shape distribution of the deposited metals might be due to the different metal/oxide interactions at the interface due to lattice oxygen transfer by the oxophilicity [41], fluxional behavior [30], and formation of bimetallic compounds [42]. In all the cases, we could see the faint In_2O_3 grain structures beneath the catalyst layer. However, the grain patterns of In_2O_3 films disappeared under the thicker catalyst layer, as shown in Fig. S2(d)-(f) for the surface morphologies with 1, 3, and 5 nm-thick Pd coating, respectively.

In addition, we measured X-ray reflectivity (XRR) of pristine In_2O_3 thin films and 1 nm Au, Pt, and Pd-coated In_2O_3 thin films (Fig. S3). The clear Kiessig fringes [43] of all samples indicates the uniformity of the

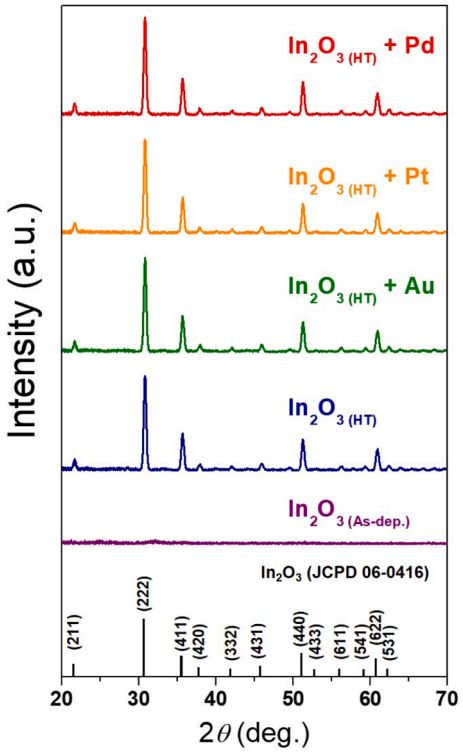

Fig. 4. XRD patterns of the as-deposited, heat-treated, and Au-, Pt-, and Pd-coated In_2O_3 thin films. The standard XRD pattern of the cubic phase of In_2O_3 (JCPD 06–0416) is shown as vertical lines at the bottom.

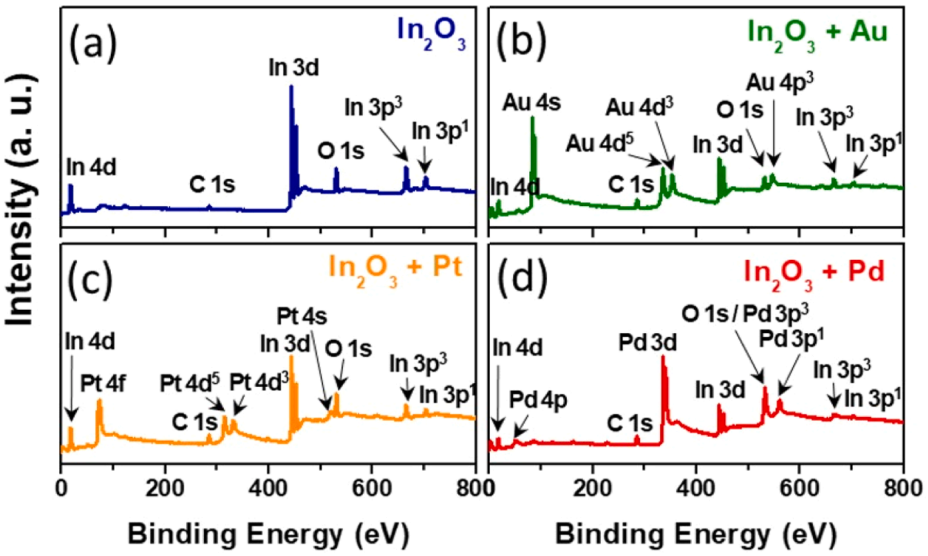

Fig. 5. Wide scan XPS spectra of (a) the bare, (b) Au-coated, (c) Pt-coated, and (d) Pd-coated In_2O_3 thin films.

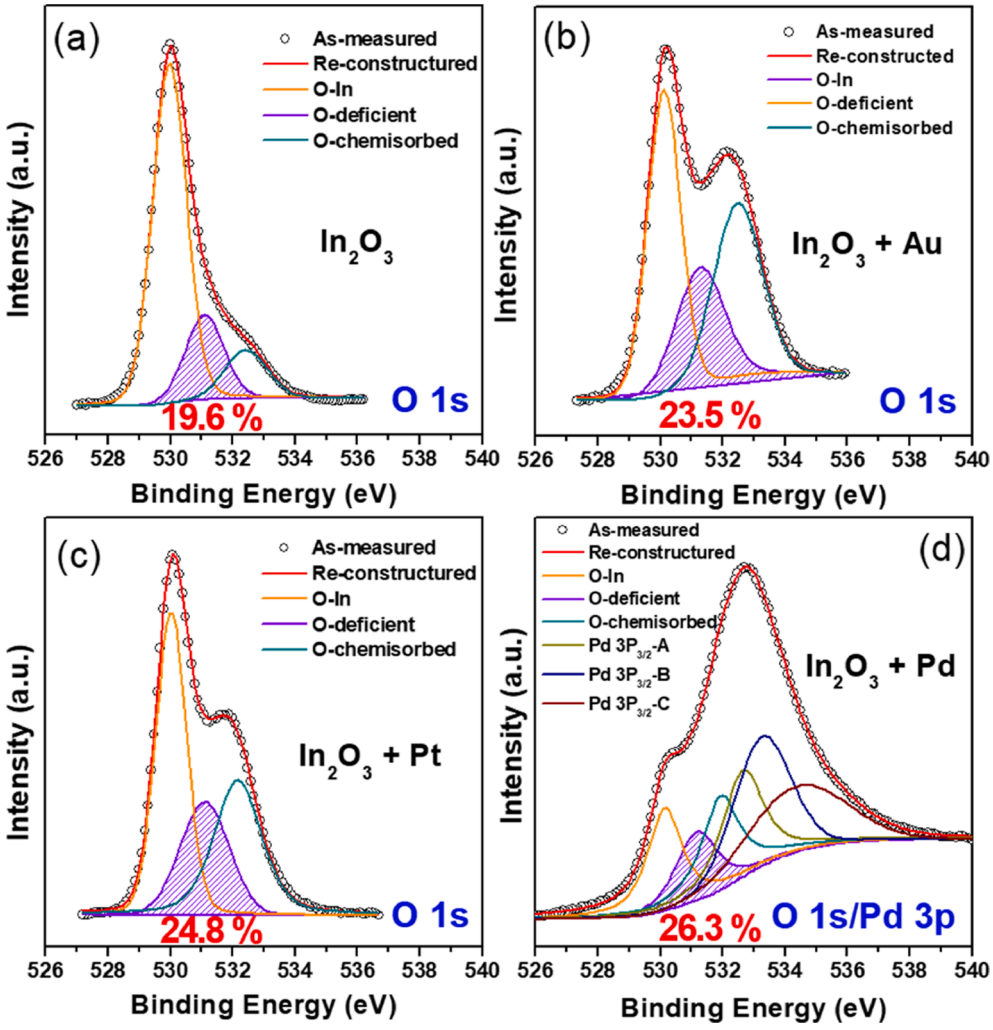

Fig. 6. Deconvoluted XPS O 1 s spectra of (a) the bare, (b) Au-coated, (c) Pt-coated, and (d) Pd-coated In_2O_3 thin films. The percentage of the oxygen-deficient peaks are marked in the panels.

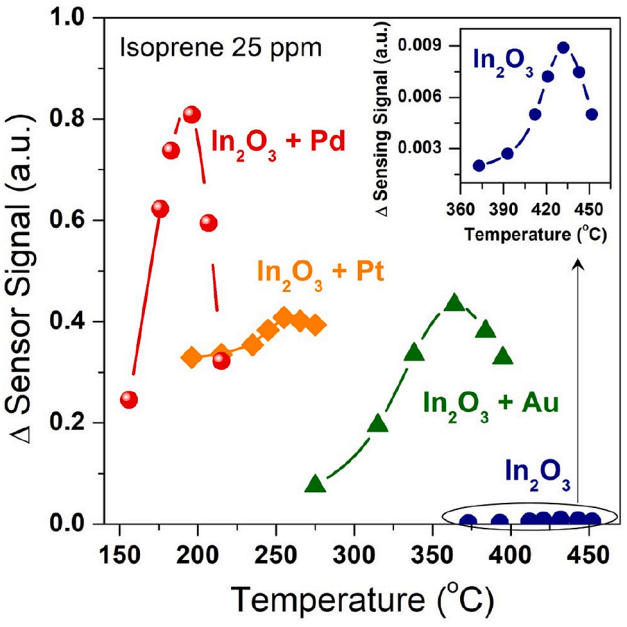

Fig. 7. Sensing response (Δ sensor signal) of the device at 25 ppm isoprene as a function of operating temperature. The inset presents a zoom in the results for the bare In_2O_3 film. Here, the sensing response of the device was defined as Δ sensor signal that means a peak height of the sensor signal (Δ sensor signal = $\log(R_{air}/R_{gas})$).

overall film thickness. From the spectra, the average thickness of In_2O_3 films was estimated to be 40 ± 2 nm, which is in good agreement with TEM images (Fig. 3). In particular, the distinct second oscillations in Au-coated In_2O_3 film (Fig. S3(b)) reveal the thicker Au layer than 1 nm, which also coincide with TEM (Fig. 3) and SEM (Fig. S2(a)) images showing irregular island shaped, self-assembled Au on the surface. In Pt and Pd-coated In_2O_3 films (Fig. S3(c) and (d)), however, XRR profiles show weak second oscillations, suggesting that Pt and Pd particles do not affect overall film thickness or surface roughness of the samples.

We further characterized the as-prepared films to understand structural properties clearly through the AFM (Fig. S4). The height distribution of deposited metals was measured using a standard tapping mode. In the SEM data, the surface of the bare In_2O_3 is consisted of many crystal grains. In AFM images, each grain was distinguished by blunt boundaries having a slightly lower height than the crystal area. When the 1 nm of Au was deposited on this surface, a high density of clusters was formed irregularly, whole over the area (Fig. S4(b)), as observed in SEM images (Fig. S2(a)). There were no significant differences after Pt deposition (Fig. S4(c)). In the case of Pd deposition, we could see the approximately 1 nm depth of valleys. Those valleys seem to be formed along with grain boundaries of the In_2O_3 beneath the Pd layer, forming replicated grains of Pd ((Fig. S4(d)). These gaps were gradually filled when further Pd was deposited, and we could not observe further grains at 5 nm Pd-coated In_2O_3 because excess Pd filled the gap (Fig. S4(f)).

Based on these AFM images, we roughly estimated the roughness (Fig. S4(g)) and surface area (Fig. S4(h)) of each film. Since metals are randomly deposited on the surface, the roughness of the metal-coated films increased compared to bare In_2O_3 (~0.17 nm), and Au-In_2O_3 showed the highest roughness (~0.4 nm) due to the large sizes of Au clusters. For the surface area, we could not normalize it in unit weight as like BET analysis. We alternatively extracted 2 μm × 2 μm region and calculated how the three-dimensional surface area was different from the two-dimensional projected area (A_{3D}/A_{2D}). Like the roughness of the films, the surface area of Pt-coated film (0.127 %) was similar or slightly less than bare In_2O_3 (0.198 %), and Au- and Pd-coated films showed an increase in the surface area, 1.14 % and 0.249 %, respectively. The higher surface area of Au is also due to the large clusters of Au particles. These morphology differences along the loaded metal species might be caused by the interfacial stability and interaction between In_2O_3 crystal and loaded metals.

To examine the crystallographic structure of the as-deposited, heat-treated, and Au-, Pt-, and Pd-coated In_2O_3 thin films, we performed XRD analysis (Fig. 4). The as-deposited In_2O_3 thin film did not exhibit a noticeable diffraction peak, confirming its amorphous phase. The heat-treated and catalyst-coated In_2O_3 thin films showed clear diffraction peaks that matched the cubic phase of In_2O_3 (JCPD 06–0416) and no signs of secondary phases or impurities. In addition, we did not observe diffraction peaks of the metal catalysts (Au, Pt, and Pd) in the catalyst-coated samples. This is likely due to the nanocrystalline phases of the catalysts, as observed in the TEM (Fig. 3(b)), SEM (Fig. S2), and AFM (Fig. S4) images.

To investigate the chemical composition of the elements in the In_2O_3 films, we performed XPS analysis in the range of 0–800 eV (Fig. 5). The observed peaks could be ascribed to In and O, as well as to Au, Pt, or Pd in the catalyst-coated films (Fig. 5(a)-5(d)). C1s peaks were also observed at a binding energy of 284.6 eV in all samples because of the unavoidable adsorption of carbon dioxide, natively residing in the air atmosphere. Since the intensities of the C1s peaks were very low compared to the main peaks, we did not take into account the effect of adsorbed carbon on the sensing performance. Furthermore, no additional peaks were observed, which confirms the single phase of the samples and is in good agreement with the XRD results (Fig. 4).

To investigate the oxidation states of the fabricated films, we deconvoluted the O1s XPS spectra (Fig. 6) into three quasi-Gaussian peaks, indicating three species of bonding. The binding energies at ~ 530 eV, ~531 eV, and ~ 532 eV correspond to the O^{2-} ions in the In-O bond of the In_2O_3 lattice, deficient oxygen in the In_2O_3 matrix, and chemisorbed oxygen species, such as adsorbed H_2O or O_2, on the surface of In_2O_3, respectively [37,38]. In the spectra of the Pd-coated In_2O_3 film, the O1s peak overlapped with the Pd 3P peak centered at ~ 532.7 eV (Fig. 6(d)). Through deconvolution, we found that the Pd 3P peak included three kinds of Pd $3P_{3/2}$ bonding species.

Among the oxygen bonding states, the deficient oxygen (~531 eV) significantly affects the gas-sensing performance [44]. The oxygen vacancies are main intrinsic defects present on the surface of this kind of MOS materials and are naturally generated by various methods during material synthesis and/or subsequent heat treatment [45–48]. The number of oxygen vacancies can be estimated by determining the area fractions of the oxygen-deficient peak in the deconvoluted O 1 s spectra [49]. This was approximately 19.6%, 23.5%, 24.8%, and 26.3% for the bare, Au-, Pt-, and Pd-coated In_2O_3 films, respectively. The deficient oxygen content of catalyst-coated In_2O_3 films was higher than that of the bare In_2O_3 films.

Unveiling the oxygen vacancy formation mechanism experimentally is extremely challenging; however, several DFT studies have been reported to address the formation of vacancies at the interface and perimeter sites of metal clusters. First, the high work function of noble metals can reduce the formation energy of oxygen vacancies and stabilize the vacancies. In our study, the work functions of Au (5.35 eV), Pt (5.37 eV), and Pd (5.44 eV) were higher than that of In_2O_3 (5.0 eV). Here, a high work function metal favors capturing more electron density to stabilize, so the noble metal prefers oxygen vacancy sites because they act as electron donors. In other words, noble metal clusters significantly lower the vacancy formation energy of oxides, producing more oxygen vacancies around the metal cluster. Several DFT calculations have proven that the oxygen vacancy formation energy is significantly reduced at the perimeter sites of the metal cluster [30]. Second, the oxophilicity of the noble metal promotes the formation of oxygen vacancies. Noble metals and oxides have a large oxophilicity gap; therefore, lattice oxygens in the oxide can be easily transferred toward metals through the metal/oxide interfaces by thermodynamic driving forces. This type of fluxional behavior has been described by DFT calculations

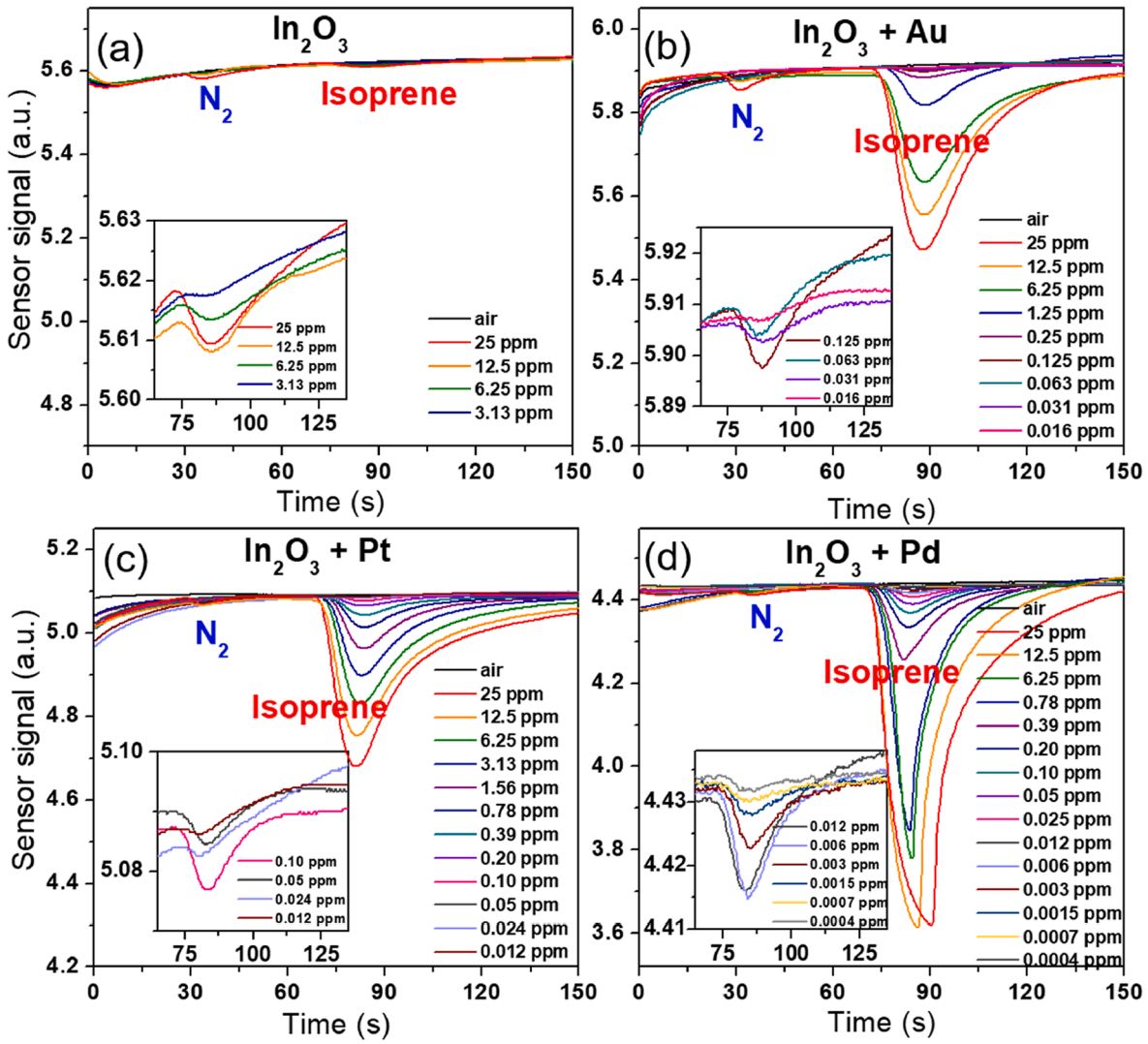

Fig. 8. Variation in the sensor signal of (a) the bare, (b) Au-coated, (c) Pt-coated, and (d) Pd-coated In_2O_3 thin films exposed to various isoprene concentrations (0.0004–25 ppm) at their optimal operating temperatures of 432℃, 364℃, 255℃, and 196 °C, respectively. The insets show a magnified plot of the isoprene sensing peak for low concentration of isoprene.

based on the interfaces between Pd clusters and the reducible oxide AgO_x [41]. The calculations showed that the oxygen in the oxide lattice was transferred to the Pd layer, producing Pd-O oxide compounds by an auto-oxidation reaction, even at 25 ℃. This oxygen transfer could also be observed at the Pd/In_2O_3 interfaces because Pd strongly interacts with In_2O_3, forming Pd/In bimetallic compounds [42,50]. The transferred oxygen atoms in Pd move towards thermodynamically active positions such as the edge of the cluster. Since the oxophilicity of metals is determined by their effective nuclear charge and electronegativity, the oxophilicity trend is presumably Pd > Pt > Au. The formation of oxygen vacancies in metal-coated oxides was also experimentally demonstrated. Cheng *et al.* reported an increase in oxygen vacancies by decorating noble metals (Au, Ag, Pt, and Pd) on mesoporous In_2O_3 [51]. According to their data (HR-TEM, XRD, and XPS), Au, Ag, and Pt remained in their metallic phase, but Pd appeared to be in the Pd^{2+} ion phase, forming oxide components by obtaining oxygen from In_2O_3. Their XPS results showed that oxygen vacancy of In_2O_3 (34.7%) significantly increased when Pd was coated (54.8 %) compared to other metals Au (38.3%), Ag (42.5%), and Pt (33.8%).

After material characterizations, we evaluated the isoprene sensing performance of the as-prepared In_2O_3 films using a mini-GC device (Fig. 2). To determine the optimal working temperature, we exposed 25 ppm of isoprene to sensors at increasing temperatures and measured the peak height (Δ sensor signal) of the sensor signal curves (Fig. 7). The optimal working temperatures for the bare In_2O_3, Au-, Pt-, and Pd-coated films were 432 °C, 364 °C, 255 °C, and 196 °C, respectively. The optimal working temperatures of the In_2O_3 films were lowered when loaded with a catalyst and were most significantly reduced for the Pd-coated film.

To further evaluate the sensitivity of the sensors, we analyzed the changes in the sensor signal over time, which were measured at their optimal working temperature at different isoprene concentrations in the range of 0.0004–25 ppm in dry air (Fig. 8). All In_2O_3 films showed a small sensing peak at ~ 34 s, corresponding to the detection of weakly interactive non-polar and small molecules of N_2 in air, and a considerably larger peak at ~ 86 s, corresponding to isoprene. This peak separation indicates that isoprene can be selectively detected in an air atmosphere using a mini-GC device integrated with In_2O_3 thin film gas sensors. The inset of Fig. 8 shows a magnified plot of the isoprene sensing peak for a low concentration of isoprene. With increasing isoprene concentration, the isoprene peak increased. Furthermore, Fig. 8 shows that catalyst-coated In_2O_3 thin films had superior sensing performances compared to bare In_2O_3 thin films.

To quantify the sensing abilities of the samples, we calculated the

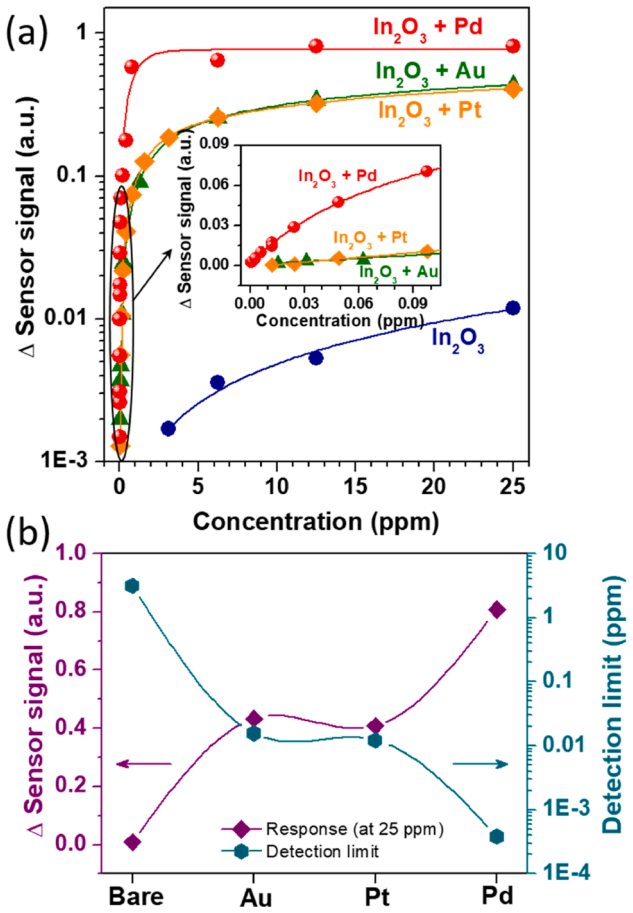

Fig. 9. (a) Sensing response (Δ sensor signal) of the bare, Au-coated, Pt-coated, and Pd-coated In_2O_3 thin films to different concentrations of isoprene in the range of 0.0004–25 ppm at their optimal operating temperatures of 432℃, 364℃, 255℃, and 196 °C, respectively. The inset presents a zoom of the sensor response for isoprene concentrations below 0.1 ppm.; (b) Summary of the sensing response at 25 ppm isoprene and lowest detection limit of isoprene of the bare and catalyst-coated In_2O_3 films.

peak heights of the Δ sensor signal at various isoprene concentrations (Fig. 9(a)). The inset of Fig. 9(a) presents an enlarged view of the Δ sensor signal at a low concentration of isoprene below 0.1 ppm. As shown in Fig. 9(a), all In_2O_3 films showed an increased peak height with an increase in isoprene concentration. We found that the Pd-coated In_2O_3 film had the best sensing performance over the entire range of concentrations. At 25 ppm isoprene, the sensing response of the Pd-coated In_2O_3 film (~0.8) was approximately 80 times higher than that of the bare In_2O_3 film (~0.01) and approximately twice higher than that of the Au- and Pt-coated In_2O_3 films (~0.4) (Fig. 9(b)). The Pd-coated In_2O_3 film also exhibited the lowest limit for isoprene detection (0.4 ppb), which is the lowest level achieved for the detection of isoprene to date. The detection limits for the bare In_2O_3 film and the Au- and Pt-coated In_2O_3 films were approximately 3.13, 0.016, and 0.012 ppm, respectively. We found that the Pd-coated In_2O_3 film showed the highest sensing response with the lowest detection limit and lowest optimal working temperature of all tested samples.

We further studied how the noble-metal loading affected improvement of the gas sensing performances. According to the general sensing mechanism of the MOS sensor, the higher sensing performance is closely related to an increase in the thickness of the electron depletion layer in the initial state (i.e., the exposed state in air). The thicker depletion layer is attributed to the large number of released electrons resulting from the large number of oxygen vacancies. In clean air, oxygen molecules trap donor electrons of oxygen vacancies and chemisorb into oxygen ions (e.g., O_2^-, O^-, or O^{2-}) on the surface of the sensing material [52]. The adsorbed oxygen ions act as reaction sites for the sensing materials when exposed to the target gas [44]. Therefore, the more oxygen vacancies are formed, the higher the gas sensing performance is improved. However, in our study, the oxygen vacancy density of each film had only 1 ~ 2 % difference, which was insufficient to fully address the dramatic change of sensing performances depending on the noble metals.

The enhanced gas-sensing performance is mainly attributed to the heterogeneous catalytic behavior of the metal/oxide interfaces. Many studies have reported that the catalytic effect of noble metals (Au, Pt, and Pd) on hydrocarbon decomposition can occur below the temperature of 500 ℃ which is overlapped with the operating temperature of our gas sensors [53,54]. These noble metals are known to activate the C-H, H-H, and C-C bonds of gas-phase hydrocarbons [55–57], promoting oxidation, dehydrogenation, and hydrogenation depending on the catalyst facet, ionic phase, atmosphere, and adsorbed molecules. Since dehydrogenation (to C-H bond cleavage), and oxidation (to transform to CO_2) reactions are required to completely decompose isoprene molecules, we deduced that loading of noble-metals significantly lowered the required energy for isoprene oxidation compared to the bare In_2O_3. However, because there are few studies on the complete oxidation of isoprene molecules using an oxide-supported noble metal catalyst, we referred to simple studies based on CO and hydrocarbons oxidation/combustion on noble metal species to understand the catalytic behavior [55,58–64].

When Au is deposited onto an In_2O_3 thin film, the majority of Au atoms prefer to exist in the metallic phase (Au^0). We found a few ionized Au species in our XPS deconvolution data, presumably located at the metal/oxide interfaces due to the interaction between metal atoms and the oxide lattice (Fig. S5(a)). When the Au catalyst is exposed to a high-temperature environment, gas-phase oxygen molecules are chemisorbed

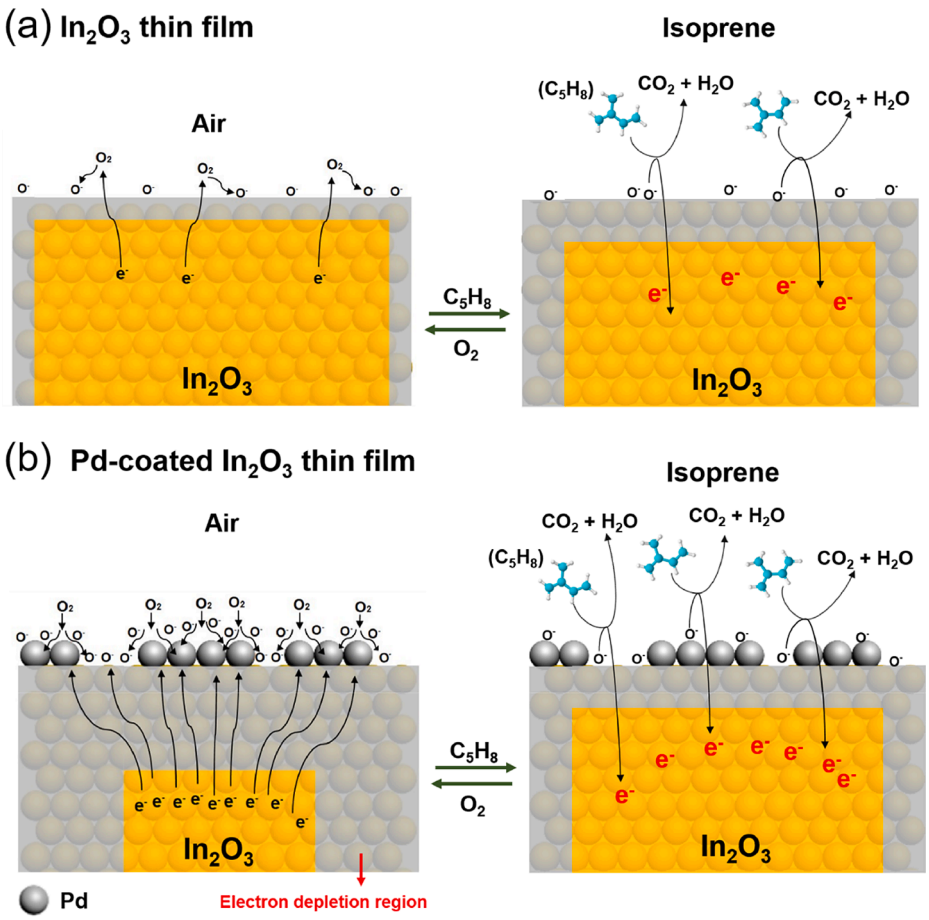

Fig. 10. Scheme illustrating the sensing reaction mechanism of (a) bare In_2O_3 film and (b) Pd-coated In_2O_3 film sensors upon exposure to air (left) and isoprene (right).

and dissociated onto the surface of the Au clusters because of the high charge density. After hydrocarbons are independently adsorbed on the Au surface, the chemisorbed oxygen species react with hydrocarbons, resulting in an oxidation reaction (Langmuir-Hinshelwood mechanism). Because the hydrocarbon and oxygen molecules competitively occupy the adsorption sites of the Au catalyst, the catalytic activity is significantly reduced when the atmosphere is oxygen-rich condition. However, in the case of a heterogeneous Au catalyst on oxide surfaces, the In_2O_3 lattice oxygen at the perimeter sites of Au catalysts can participate in the oxidation reaction with adsorbed hydrocarbons on the Au cluster via the Mars-van-Krevelen mechanism [60]. After the reaction, the consumed oxygen sites become oxygen vacancies, which are refilled by gas-phase oxygen molecules for further reactions. Pt has a tendency similar to that of the Au catalyst whereby Pt prefers to exist in the metallic phase at room temperature. Likewise, when the Pt catalyst is deposited on the oxide surface, the interfacial Pt atoms are transformed into ionic species due to Pt-O-In bonding (Fig. S5(b)). Since Pt has few or no oxygen atoms in the lattice, the catalytic reaction on the Pt surface is dominantly conducted via the Langmuir-Hinshelwood mechanism between surface adsorbed oxygen atoms and hydrocarbons. However, oxide-supported Pt catalysts exhibit heterogeneous catalytic behavior at the metal/oxide interfaces, as like the Au catalyst. The In_2O_3 lattice oxygens at the perimeter of the Pt clusters also participate in the catalytic reaction by reacting with adsorbed hydrocarbons on the Pt surfaces. The related oxidation reaction was experimentally proven by operando TEM using a Pt/CeO_2 heterogeneous catalyst [62].

Unlike Au and Pt, Pd is stable in the oxide phase (PdO) under 800 °C [61]. When the Pd catalyst was deposited on the In_2O_3 thin film, the lattice oxygen in In_2O_3 was transferred to Pd even at 25 ℃, due to the oxophilicity differences, as previously described in the oxygen vacancy formation mechanism [41]. The XPS results also showed a high proportion of the Pd^{2+} phase in the Pd 3d peak (Fig. S5(c)), indicating the presence of PdO phases. According to previous studies, these PdO_{1-x} compounds actively participate in C-H bond cleavage and oxidation reactions by Mars-van-Krevelen mechanisms, taking advantage of lattice oxygen. Interestingly, the consumed lattice oxygen sites can be rapidly refilled by gas-phase oxygen molecules because of the thermodynamically favored conformation of the PdO structure, reoxidizing Pd into PdO. This efficient reduction-reoxidation process of PdO promotes a much higher catalytic reaction efficiency than other noble metals because the reoxidation step is the rate-determining step of the Mars-van-Krevelen mechanism [65]. This phenomenon was proven in another study, which reported a decrease in the catalytic reaction temperature with a significant enhancement in the CH_4 conversion rate on the Pd/SnO_2 heterogeneous catalyst [64].

Based on these mechanism studies, the effects of metal coating on gas sensing performance can be explained by the number of active sites for the catalytic reaction. According to the reaction mechanism, Pd-coating produced the most abundant active sites for oxidation reaction owing to the formation of PdO compounds, which directly participate in the oxidation reaction by the Mars-van-Krevelen mechanism. On the other hand, in cases of the Au- and Pt-coated In_2O_3 thin films, only perimeter sites of metal catalysts were active for the oxidation reaction. In the same manner, when we compare the Au- and Pt-coating, higher sensing performance is expected at Pt-coating because the size of the metal cluster is much smaller than that of Au, as shown in Fig. S2. The bigger the cluster size is, the less active sites exist due to the decrease of perimeter sites. Therefore, we could predict the tendency of gas sensing

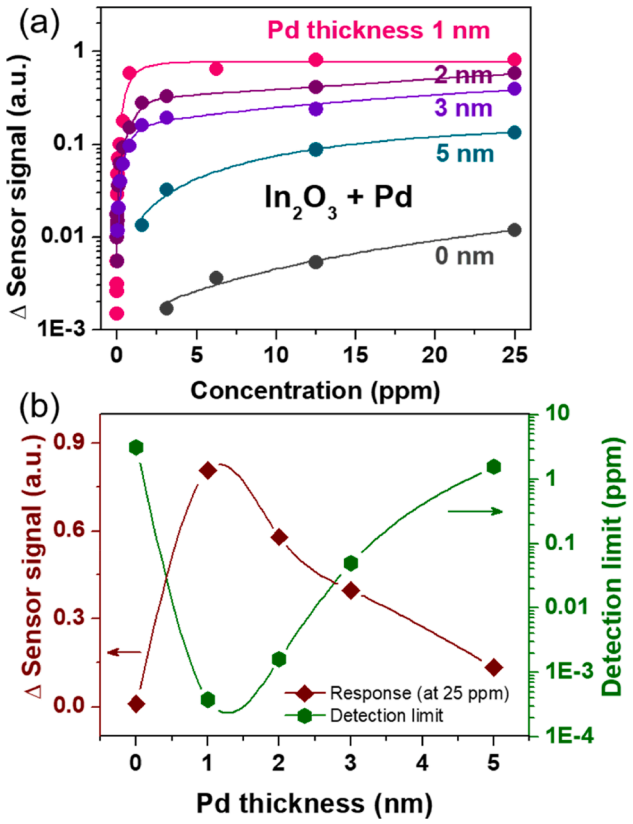

Fig. 11. (a) Sensing response (Δ sensor signal) of the bare In_2O_3 film ($d = 0$) and the various Pd-coated In_2O_3 films with different Pd thickness ($d = 1$, 2, 3, and 5 nm) to different isoprene concentrations at their optimal working temperatures of 432℃ and 196℃, respectively.; (b) Summary of the sensing response at 25 ppm isoprene and lowest detection limit of isoprene for the different Pd thickness of Pd-coated In_2O_3 films.

Table 1
ICP-OES analysis of In_2O_3-based thin films.

Samples	In		Pd		Weight percent (%) (In : Pd, w/w)
	Weight (μg/g)	*RSD (%)	Weight (μg/g)	*RSD (%)	
Bare In_2O_3	161.97	3.46	–		–
Pd 1 nm	158.08	1.07	9.99	0.78	6.32
Pd 3 nm	157.83	3.22	29.05	1.25	18.41
Pd 5 nm	155.37	1.15	47.02	0.76	30.26

*RSD : Relative standard deviation

performances as Pd- > Pt- > Au-coated In_2O_3 thin films. However, although we roughly interpret the catalytic activity based on the active sites of catalytic behavior, the direct comparison of gas sensing performances remains elusive because the catalytic effects are dependent on various factors, such as the catalyst facet, oxidation states, size of the cluster, and metal/oxide interface. In addition to that, metal catalysts contribute to an increase in oxygen vacancies, the formation of a thick electron depletion layer by charge exchange based on work function differences, and the spill-over effect [66]. Those factors have synergistic effects on gas sensing mechanisms, so further fundamental studies are required to clearly understand the influence of the metal coating on gas sensing.

The sensing mechanisms of isoprene are briefly illustrated in Fig. 10. When the sensing materials are heated up to optimal working temperature, oxygen molecules are ionized on the surface of the catalysts and In_2O_3 thin films by accepting donor electrons of oxygen vacancies, forming the electron depletion layers. After being exposed to isoprene, a sensing reaction occurs between isoprene and the adsorbed oxygen ion species. At the working temperature of the In_2O_3 film (100 °C ≤ T ≤ 300 °C), the isoprene can be completely oxidized, according to the following equation:

$$C_5H_{8(ads)} + 14O^-_{(ads)} \rightarrow 5CO_{2(gas)} + 4H_2O_{(gas)} + 14e^- \quad (2)$$

Consequently, a large number of electrons return to the conduction band of the In_2O_3, resulting in a decrease in the depletion layer thickness (Fig. 10 (right)) and the resistance of the film (Fig. 8). Therefore, the thicker depletion layer of the Pd-coated In_2O_3 film leads to a greater resistance reduction when exposed to isoprene than that of the pure In_2O_3 films (Fig. 8(d)).

To optimize the sensing performance of the Pd-coated In_2O_3 film, we evaluated the sensing responses of Pd-coated In_2O_3 films prepared with Pd thicknesses of d = 1–5 nm at an optimal working temperature of 196 °C for different isoprene concentrations (0.0004–25 ppm) (Fig. 11 (a)). They were compared with those of the bare In_2O_3 film ($d = 0$) at the optimal working temperature of 432 °C. The sensing performances of the various Pd-coated In_2O_3 films are summarized in Fig. 11(b). The sensing peak heights of 25 ppm isoprene for $d = 0$, 1, 2, 3, and 5 nm were approximately 0.009, 0.808, 0.580, 0.397, and 0.133, respectively. The lowest limits of isoprene detection for d = 0, 1, 2, 3, and 5 nm were approximately 3.13, 0.0004, 0.0016, 0.049, and 1.56 ppm, respectively. Hence, the Pd-coated In_2O_3 films with a Pd thickness of 1 nm exhibited the best isoprene sensing performance.

We conducted a quantitative analysis of fabricated thin films to understand how the film composition affects the sensing performance. For the measurement, bare In_2O_3 and Pd 1 nm, 3 nm, and 5 nm loaded In_2O_3 thin films were fabricated on a Si/SiO_2 substrate. The entire samples were totally digested in the aqua regia, and aliquots of the resultant solutions were sampled in the ICP-OES. The measurement was repeated several times for reliability, and the relative standard deviation (RSD) of each result was calculated (Table 1). As expected, the absolute amount

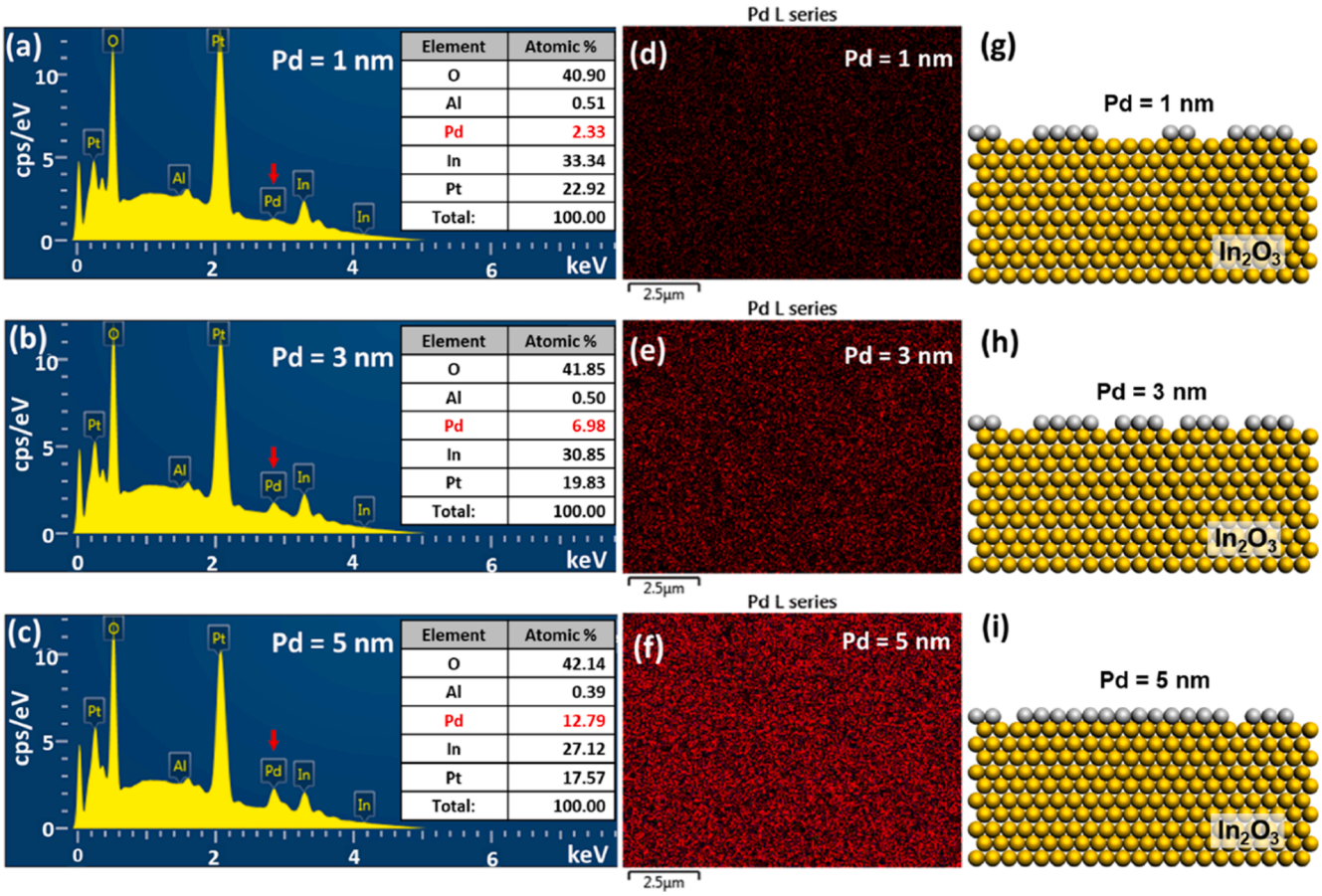

Fig. 12. (a)-(c) EDS spectra obtained from point analyses averaged at different positions of samples with different Pd thickness of 1, 3, and 5 nm; (d)-(f) EDS elemental color mapping images for Pd with thicknesses of 1, 3, and 5 nm; (g)-(i) Schematic view of the Pd layer distribution with increasing thickness.

of the Pd linearly increased along with the thickness of the Pd layer. Based on the results, the Pd to In weight percentage (w/w) was calculated as 6.32 %, 18.41 %, and 30.26 % for 1 nm Pd, 3 nm Pd, and 5 nm Pd loading, respectively. We confirmed that sensing performance diminished with the increase of Pd contents, but not proportionally. It means the performance is also affected by other factors, not simply by the loading amount of the precious metal. In the case of Pd-In_2O_3 thin films, PdO is a critical compound for catalytic reactions. According to DFT calculations [41], the oxygen transferred from the In_2O_3 thin film is mainly located at the edge of the Pd clusters. However, when the Pd loading increased, the sizes of the clusters also increased, eventually merging with each other and significantly reducing the edge sites of the Pd clusters. In other words, the active sites for the catalytic reaction are diminished at higher loading conditions (3 nm and 5 nm), so that the gas sensing performance is also reduced.

To confirm whether our hypothesis is reasonable, the distributions of catalytic Pd layers with thicknesses of 1, 3, and 5 nm on In_2O_3 films, we performed compositional point analyses at different positions on the samples using EDS (Fig. 12(a)–(c)) and visualized the distribution of Pd on the sample using EDS elemental color mapping (Fig. 12(d)–(f)). We found that the elemental density of Pd increased and that more Pd atoms covered the In_2O_3 film with increasing Pd thickness. Therefore, we conclude that with increasing Pd thickness, more Pd atoms covered more of the In_2O_3 surface area, filling the exposed area of In_2O_3 (Fig. 12 (g)–(i)). These results also agreed with the SEM and AFM data. We previously explained that Pd transitions to PdO by obtaining oxygens from the In_2O_3, and transferred oxygens are located at edge sites of Pd clusters. When the clusters grow up by depositing the excess amount of Pd, then the fraction of edge sites decreases, whereby oxygen coverage, used to hydrocarbon oxidation reaction, is reduced too. In other words, when the Pd thickness increased above 1 nm, fewer active sites were available on the film, which decreased the sensing performance.

Furthermore, we tested humidity effect, repeatability, and long-term stability of the Pd-coated In_2O_3 film incorporated into the mini-GC at an optimal operating temperature of 196 °C. Fig. 13(a) shows the humidity effect on the sensitivity in the range of 0.01–10 ppm isoprene under various humid conditions. The values of Δ sensor signal for various conditions were obtained from the sensor signal curves shown in Fig. S6 (a)-(c). The sensitivity (slope) decreases at 90 RH%. However, the lower detection limit of 0.01 ppm is still maintained even under a high humid condition. It is also noteworthy that the sensitivity hardly changed when 90 RH% of isoprene gas was passed through the membrane moisture filter. For the repeatability test of the Pd-coated In_2O_3 film, the sensor signals were measured continuously with exposure to 25 ppm isoprene at 196 °C for 40 cycles (Fig. S6(d)). Fig. 13(b) presents that the sensing response was not significantly lowered and was almost constant. The long-term stability of the Pd-coated In_2O_3 film was also tested by exposing 25 ppm isoprene at an optimal operating temperature of 196 °C under dry air conditions. Fig. 13(c) shows the change in the Δ sensor signal with time, which was measured at intervals of 5 or 10 days for 60 days. The sensor temperature was raised only when the response was measured, and then it was maintained at room temperature. As shown in Fig. 13, the sensor response decreased by ~ 16% after 30 days and became saturated for 60 days within the error range. The results indicate that the Pd-coated In_2O_3 film mounted on the mini-GC achieved good repeatability and long-term stability for the detection of 25 ppm isoprene, and there is no sensing effect by moisture when the moisture filter is adopted.

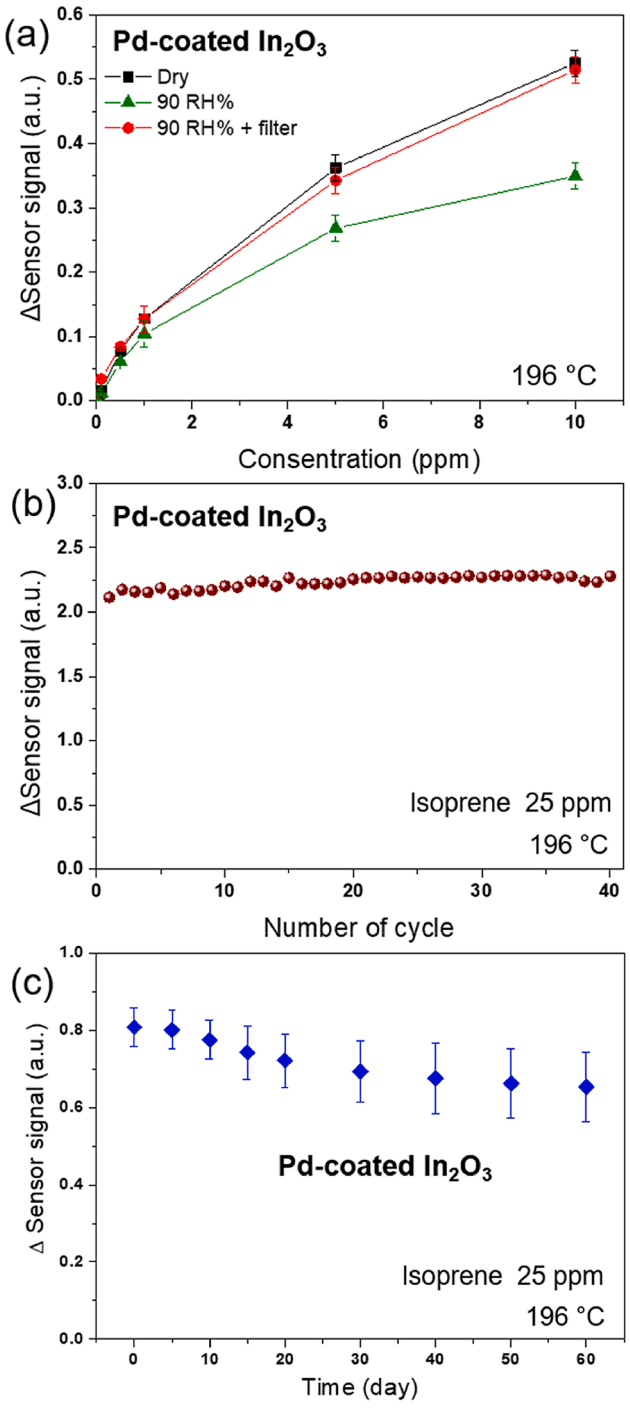

Fig. 13. Sensing performance of Pd-loaded In_2O_3 film incorporated into the mini-GC: (a) Humidity effect on sensitivity in the range of 0.01–10 ppm isoprene under conditions without humidity(dry), with 90% RH, and with 90% RH passed through moisture filter at 196 °C; (b) Repeatability test in sensing 25 ppm isoprene over 40 cycles at 196 °C; (c) A long-term stability for 25 ppm isoprene at 196 °C measured at an interval of 5 or 10 days for 60 days.

4. Conclusions

We designed highly sensitive isoprene sensors based on In_2O_3 films and evaluated their sensing performance using our portable analyzer equipped with a mini-GC column for practical application as a breath isoprene analyzer. To improve the sensing performance, the In_2O_3 thin film was grown uniformly with high crystallinity and better compositional stoichiometry using DIBS film deposition method. The surface defects such as oxygen vacancies, which significantly affect the sensing performance of the MOS-based sensor, were controlled by loading metal catalysts (Au, Pt, and Pd) on the film surface. We observed a significant enhancement in the gas-sensing performance of the noble metal-coated thin films. Among the tested samples, the Pd-coated In_2O_3 film showed the best isoprene sensing performance. Within 100 s, the sensor was able to selectively detect isoprene as low as 0.4 ppb concentration in air at a low operating temperature of 196 °C. This is the best isoprene sensing performance ever reported. We interpret that this enhanced sensing activity is attributed to the increase in oxygen vacancies, formation of stable PdO compounds by obtaining oxygen from the In_2O_3 lattice, efficient reduction-reoxidation of PdO, and the Mars-van-Krevelen mechanism on the PdO surfaces. We further optimized the isoprene sensing performance of the Pd-coated In_2O_3 film by varying the Pd thickness and found that thickness of 1 nm showed the optimal status of discontinuous islands for sensing. Therefore, our results demonstrate that the mini-GC device integrated with the Pd-coated In_2O_3 film can be utilized to detect isoprene rapidly and accurately in breath.

CRediT authorship contribution statement

Hwaebong Jung: Conceptualization, Investigation, Visualization, Writing – original draft. **Hyegi Min:** Investigation, Visualization, Writing – original draft, Writing – review & editing. **Junho Hwang:** Investigation, Visualization. **Jihee Kim:** Investigation, Visualization. **Yong-Sahm Choe:** Conceptualization, Validation. **Hyun-Sook Lee:** Conceptualization, Validation, Writing – original draft, Writing – review & editing. **Wooyoung Lee:** Conceptualization, Supervision.

Declaration of Competing Interest

The authors declare that they have no known competing financial interests or personal relationships that could have appeared to influence the work reported in this paper.

Acknowledgments

This research was supported by the Basic Science Research Program (2017M3A9F1052297) and the Priority Research Centers Program (2019R1A6A1A11055660) through the National Research Foundation of Korea (NRF), funded by the Korean government (Ministry of Science and ICT) and the Technology Innovation Program ('20013621', Center for Super Critical Material Industrial Technology) funded by the Ministry of Trade, Industry & Energy (MOTIE, Korea). H.-S. Lee thanks the Basic Research in Science and Engineering Program of NRF (2021R1A2C1013690). H. Min thanks the Korea Initiative for fostering University of Research and Innovation Program of NRF (2020M3H1A1077207).

Appendix A. Supplementary material

Supplementary data to this article can be found online at https://doi.org/10.1016/j.apsusc.2022.152827.

References

[1] M. Phillips, J. Herrera, S. Krishnan, M. Zain, J. Greenberg, R.N. Cataneo, Variation in volatile organic compounds in the breath of normal humans, J Chromatogr B 729 (1-2) (1999) 75–88.
[2] A. Amann, G. Poupart, S. Telser, M. Ledochowski, A. Schmid, S. Mechtcheriakov, Applications of breath gas analysis in medicine, International Journal of Mass Spectrometry 239 (2-3) (2004) 227–233.
[3] T. Karl, P. Prazeller, D. Mayr, A. Jordan, J. Rieder, R. Fall, et al., Human breath isoprene and its relation to blood cholesterol levels: new measurements and modeling, Journal of Applied Physiology 91 (2001) 762–770.
[4] P. Španěl, S. Davies, D. Smith, Quantification of breath isoprene using the selected ion flow tube mass spectrometric analytical method, Rapid communications in mass spectrometry 13 (17) (1999) 1733–1738.

[5] J.P. Conkle, B.J. Camp, B.E. Welch, Trace composition of human respiratory gas, Archives of Environmental Health: An, International Journal 30 (1975) 290–295.

[6] J. King, A. Kupferthaler, K. Unterkofler, H. Koc, S. Teschl, G. Teschl, W. Miekisch, J. Schubert, H. Hinterhuber, A. Amann, Isoprene and acetone concentration profiles during exercise on an ergometer, Journal of breath research 3 (2) (2009) 027006, https://doi.org/10.1088/1752-7155/3/2/027006.

[7] S. Davies, P. Španel, D. Smith, A new 'online'method to measure increased exhaled isoprene in end-stage renal failure, Nephrology Dialysis Transplantation 16 (4) (2001) 836–839.

[8] A. Bajtarevic, C. Ager, M. Pienz, M. Klieber, K. Schwarz, M. Ligor, T. Ligor, W. Filipiak, H. Denz, M. Fiegl, W. Hilbe, W. Weiss, P. Lukas, H. Jamnig, M. Hackl, A. Haidenberger, B. Buszewski, W. Miekisch, J. Schubert, A. Amann, Noninvasive detection of lung cancer by analysis of exhaled breath, BMC cancer 9 (1) (2009), https://doi.org/10.1186/1471-2407-9-348.

[9] A. Mashir, K.M. Paschke, D. van Duin, N.K. Shrestha, D. Laskowski, M.K. Storer, B. Yen-Lieberman, S.M. Gordon, M. Aytekin, R.A. Dweik, Effect of the influenza A (H1N1) live attenuated intranasal vaccine on nitric oxide (FENO) and other volatiles in exhaled breath, Journal of breath research 5 (3) (2011) 037107, https://doi.org/10.1088/1752-7155/5/3/037107.

[10] J. King, P. Mochalski, A. Kupferthaler, K. Unterkofler, H. Koc, W. Filipiak, S. Teschl, H. Hinterhuber, A. Amann, Dynamic profiles of volatile organic compounds in exhaled breath as determined by a coupled PTR-MS/GC-MS study, Physiological measurement 31 (9) (2010) 1169–1184.

[11] M. Dolch, L. Frey, C. Hornuss, M. Schmoelz, S. Praun, J. Villinger, et al., Molecular breath-gas analysis by online mass spectrometry in mechanically ventilated patients: a new software-based method of CO_2-controlled alveolar gas monitoring, Journal of breath research 2 (2008), 037010.

[12] C. Hornuss, M.E. Dolch, S. Janitza, K. Souza, S. Praun, C.C. Apfel, G. Schelling, Determination of breath isoprene allows the identification of the expiratory fraction of the propofol breath signal during real-time propofol breath monitoring, Journal of clinical monitoring and computing 27 (5) (2013) 509–516.

[13] C. Hagleitner, A. Hierlemann, D. Lange, A. Kummer, N. Kerness, O. Brand, H. Baltes, Smart single-chip gas sensor microsystem, Nature 414 (6861) (2001) 293–296.

[14] A.T. Güntner, N.J. Pineau, D. Chie, F. Krumeich, S.E. Pratsinis, Selective sensing of isoprene by Ti-doped ZnO for breath diagnostics, Journal of Materials Chemistry B 4 (32) (2016) 5358–5366.

[15] Y. Park, R. Yoo, S. ryull Park, J.H. Lee, H. Jung, H.-S. Lee, et al., Highly sensitive and selective isoprene sensing performance of ZnO quantum dots for a breath analyzer, Sensors and Actuators B: Chemical, 290(2019) 258-66.

[16] A. Teleki, S.E. Pratsinis, K. Kalyanasundaram, P. Gouma, Sensing of organic vapors by flame-made TiO_2 nanoparticles, Sensors and actuators B: chemical 119 (2006) 683–690.

[17] T. Itoh, D. Lee, T. Goto, T. Akamatsu, N. Izu, W. Shin, et al., Analysis of Recovery Time of Pt-, Pd-, and Au-Loaded SnO_2 Sensor Material with Nonanal as Large-Molecular-Weight Volatile Organic Compounds, Sens Mater 28 (2016) 1165–1178.

[18] J. van den Broek, A.T. Güntner, S.E. Pratsinis, Highly selective and rapid breath isoprene sensing enabled by activated alumina filter, ACS sensors 3 (3) (2018) 677–683.

[19] P.-I. Gouma, L. Wang, S. Simon, M. Stanacevic, Novel isoprene sensor for a flu virus breath monitor, Sensors 17 (12) (2017) 199, https://doi.org/10.3390/s17010199.

[20] L.i. Liu, T. Zhang, S. Li, L. Wang, Y. Tian, Preparation, characterization, and gas-sensing properties of Pd-doped In2O3 nanofibers, Mater Lett 63 (23) (2009) 1975–1977.

[21] S. Elouali, L.G. Bloor, R. Binions, I.P. Parkin, C.J. Carmalt, J.A. Darr, Gas Sensing with Nano-Indium Oxides (In2O3) Prepared via Continuous Hydrothermal Flow Synthesis, Langmuir 28 (3) (2012) 1879–1885.

[22] P. Song, D. Han, H. Zhang, J. Li, Z. Yang, Q.i. Wang, Hydrothermal synthesis of porous In_2O_3 nanospheres with superior ethanol sensing properties, Sensor Actuat B-Chem 196 (2014) 434–439.

[23] X. Sun, H. Ji, X. Li, S. Cai, C. Zheng, Mesoporous In_2O_3 with enhanced acetone gas-sensing property, Mater Lett 120 (2014) 287–291.

[24] W. Yang, P. Wan, X. Zhou, J. Hu, Y. Guan, L. Feng, Self-assembled In_2O_3 truncated octahedron string and its sensing properties for formaldehyde, Sensor Actuat B-Chem 201 (2014) 228–233.

[25] F. Gu, R. Nie, D. Han, Z. Wang, In2O3-graphene nanocomposite based gas sensor for selective detection of NO_2 at room temperature, Sensor Actuat B-Chem 219 (2015) 94–99.

[26] Y. Wang, G. Duan, Y. Zhu, H. Zhang, Z. Xu, Z. Dai, W. Cai, Room temperature H_2S gas sensing properties of In2O3 micro/nanostructured porous thin film and hydrolyzation-induced enhanced sensing mechanism, Sensor Actuat B-Chem 228 (2016) 74–84.

[27] B. Huang, Z. Zhang, C. Zhao, L. Cairang, J. Bai, Y. Zhang, X. Mu, J. Du, H. Wang, X. Pan, J. Zhou, E. Xie, Enhanced gas-sensing performance of ZnO@In_2O_3 core@shell nanofibers prepared by coaxial electrospinning, Sensor Actuat B-Chem 255 (2018) 2248–2257.

[28] M. Hanada, H. Koda, K. Onaga, K. Tanaka, T. Okabayashi, T. Itoh, H. Miyazaki, Portable oral malodor analyzer using highly sensitive In_2O_3 gas sensor combined with a simple gas chromatography system, Anal Chim Acta 475 (1-2) (2003) 27–35.

[29] Q. Zheng, J.H. Lee, S.-J. Kim, H.-S. Lee, W. Lee, Excellent isoprene-sensing performance of In_2O_3 nanoparticles for breath analyzer applications, Sensors and Actuators B: Chemical 327 (2021), 128892.

[30] A.R. Puigdollers, P. Schlexer, S. Tosoni, G. Pacchioni, Increasing Oxide Reducibility: The Role of Metal/Oxide Interfaces in the Formation of Oxygen Vacancies, ACS Catal 7 (2017) 6493–6513.

[31] S.K. Pandey, S.K. Pandey, U.P. Deshpande, V. Awasthi, A. Kumar, M. Gupta, S. Mukherjee, Effect of oxygen partial pressure on the behavior of dual ion beam sputtered ZnO thin films, Semicond Sci Tech 28 (8) (2013) 085014, https://doi.org/10.1088/0268-1242/28/8/085014.

[32] S. Mukherjee, Thin film deposition from dual ion beam sputtering system, CSI Transactions on ICT 7 (2) (2019) 99–104.

[33] A.A. Daryakenari, A. Apostoluk, J.J. Delaunay, Effect of Pt decoration on the gas response of ZnO nanoparticles, physica status solidi (c), 10(2013) 1297-300.

[34] S. Gil, J. Garcia-Vargas, L. Liotta, G. Pantaleo, M. Ousmane, L. Retailleau, A. Giroir-Fendler, Catalytic Oxidation of Propene over Pd Catalysts Supported on CeO_2, TiO_2, Al_2O_3 and M/Al_2O_3 Oxides (M = Ce, Ti, Fe, Mn), Catalysts 5 (2) (2015) 671–689.

[35] T.V. Choudhary, S. Banerjee, V.R. Choudhary, Catalysts for combustion of methane and lower alkanes, Applied Catalysis A: General 234 (1-2) (2002) 1–23.

[36] S. Specchia, F. Conti, V. Specchia, Kinetic Studies on Pd/$Ce_xZr_{1-x}O_2$ Catalyst for Methane Combustion, Industrial & engineering chemistry research 49 (21) (2010) 11101–11111.

[37] S.J. Park, I. Bae, I.-S. Nam, B.K. Cho, S.M. Jung, J.-H. Lee, Oxidation of formaldehyde over Pd/Beta catalyst, Chemical engineering journal 195-196 (2012) 392–402.

[38] M. Rotko, A. Machocki, B. Stasinska, Studies of catalytic process of complete oxidation of methane by SSITKA method, Applied Surface Science 256 (17) (2010) 5585–5589.

[39] Y.-S. Choe, New gas sensing mechanism for SnO_2 thin-film gas sensors fabricated by using dual ion beam sputtering, Sensors and Actuators B: Chemical 77 (2001) 200–208.

[40] H. Jung, W. Cho, R. Yoo, H.-S. Lee, Y.-S. Choe, J.Y. Jeon, et al., Highly selective real-time detection of breath acetone by using ZnO quantum dots with a miniaturized gas chromatographic column, Sensors and Actuators B: Chemical 274 (2018) 527–532.

[41] V. Mehar, A. Almithn, T. Egle, M.-H. Yu, C.R. O'Connor, M. Karatok, R.J. Madix, D. Hibbitts, J.F. Weaver, Oxophilicity Drives Oxygen Transfer at a Palladium-Silver Interface for Increased CO Oxidation Activity, Acs Catal 10 (23) (2020) 13878–13889.

[42] N. Rui, Z. Wang, K. Sun, J. Ye, Q. Ge, C.-J. Liu, CO2 hydrogenation to methanol over Pd/In_2O_3: effects of Pd and oxygen vacancy, Applied Catalysis B: Environmental 218 (2017) 488–497.

[43] H. Kiessig, Untersuchungen zur totalreflexion von röntgenstrahlen, Annalen der Physik 402 (6) (1931) 715–768.

[44] S. Bai, T. Guo, Y. Zhao, R. Luo, D. Li, A. Chen, C.C. Liu, Mechanism enhancing gas sensing and first-principle calculations of Al-doped ZnO nanostructures, Journal of Materials Chemistry A 1 (37) (2013) 11335, https://doi.org/10.1039/c3ta11516j.

[45] S.J. Patil, A.V. Patil, C.G. Dighavkar, K.S. Thakare, R.Y. Borase, S.J. Nandre, N. G. Deshpande, R.R. Ahire, Semiconductor metal oxide compounds based gas sensors: A literature review, Frontiers of, Materials Science 9 (1) (2015) 14–37.

[46] M. Al-Hashem, S. Akbar, P. Morris, Role of oxygen vacancies in nanostructured metal-oxide gas sensors: a review, Sensors and Actuators B: Chemical 301 (2019) 126845, https://doi.org/10.1016/j.snb.2019.126845.

[47] W. Kim, M. Choi, K. Yong, Generation of oxygen vacancies in ZnO nanorods/films and their effects on gas sensing properties, Sensors and Actuators B: Chemical 209 (2015) 989–996.

[48] A. Sarkar, G.G. Khan, The formation and detection techniques of oxygen vacancies in titanium oxide-based nanostructures, Nanoscale 11 (8) (2019) 3414–3444.

[49] S. Yun, S. Lim, Improved conversion efficiency in dye-sensitized solar cells based on electrospun Al-doped ZnO nanofiber electrodes prepared by seed layer treatment, Journal of Solid State Chemistry 184 (2) (2011) 273–279.

[50] J. Ye, Q. Ge, C.-J. Liu, Effect of PdIn bimetallic particle formation on CO_2 reduction over the Pd–In/SiO2 catalyst, Chemical Engineering Science 135 (2015) 193–201.

[51] H.-Y. Lai, C.-H. Chen, Highly sensitive room-temperature CO gas sensors: Pt and Pd nanoparticle-decorated In_2O_3 flower-like nanobundles, Journal of Materials Chemistry 22 (2012) 13204–13208.

[52] M.Z. Ahmad, A.Z. Sadek, K. Latham, J. Kita, R. Moos, W. Wlodarski, Chemically synthesized one-dimensional zinc oxide nanorods for ethanol sensing, Sensors and Actuators B: Chemical 187 (2013) 295–300.

[53] O. Inderwildi, S. Jenkins, D. King, Mechanistic studies of hydrocarbon combustion and synthesis on noble metals, Angewandte chemie international edition 47 (28) (2008) 5253–5255.

[54] H.-S. Kim, H.-J. Kim, J.-H. Kim, J.-H. Kim, S.-H. Kang, J.-H. Ryu, N.-K. Park, D.-S. Yun, J.-W. Bae, Noble-Metal-Based Catalytic Oxidation Technology Trends for Volatile Organic Compound (VOC) Removal, Catalysts 12 (1) (2022) 63, https://doi.org/10.3390/catal12010063.

[55] J.F. Weaver, Surface chemistry of late transition metal oxides, Chemical reviews 113 (6) (2013) 4164–4215.

[56] M.M. Montemore, M.A. van Spronsen, R.J. Madix, C.M. Friend, O_2 activation by metal surfaces: implications for bonding and reactivity on heterogeneous catalysts, Chemical reviews 118 (2017) 2816–2862.

[57] N.M. Kinnunen, J.T. Hirvi, M. Suvanto, T.A. Pakkanen, Role of the interface between Pd and PdO in methane dissociation, The Journal of Physical Chemistry C 115 (39) (2011) 19197–19202.

[58] A.M. Ali, M.A. Daous, A. Arafat, A.A. AlZahrani, Y. Alhamed, A. Tuerdimaimaiti, L. A. Petrov, Effect of Au precursor and support on the catalytic activity of the nano-Au-catalysts for propane complete oxidation, Journal of Nanomaterials 2015 (2015) 1–10.

[59] H.Y. Kim, H.M. Lee, G. Henkelman, CO oxidation mechanism on CeO2-supported Au nanoparticles, Journal of the American Chemical Society 134 (3) (2012) 1560–1570.

[60] D. Widmann, R.J. Behm, Dynamic surface composition in a Mars-van Krevelen type reaction: CO oxidation on Au/TiO_2, Journal of catalysis 357 (2018) 263–273.
[61] E.J. Jang, J. Lee, D.G. Oh, J.H. Kwak, CH_4 Oxidation Activity in Pd and Pt–Pd Bimetallic Catalysts: Correlation with Surface PdO x Quantified from the DRIFTS Study, Acs Catal 11 (2021) 5894–5905.
[62] J.L. Vincent, P.A. Crozier, Atomic level fluxional behavior and activity of CeO_2-supported Pt catalysts for CO oxidation, Nature communications 12 (2021) 1–13.
[63] J. Ma, Y. Lou, Y. Cai, Z. Zhao, L.i. Wang, W. Zhan, Y. Guo, Y. Guo, The relationship between the chemical state of Pd species and the catalytic activity for methane combustion on Pd/CeO 2, Catalysis, Science & Technology 8 (10) (2018) 2567–2577.
[64] Z. Zhao, B. Wang, J. Ma, W. Zhan, L.i. Wang, Y. Guo, Y. Guo, G. Lu, Catalytic combustion of methane over Pd/SnO_2 catalysts, Chinese Journal of Catalysis 38 (8) (2017) 1322–1329.
[65] A.J. Schwanke, R. Balzer, S. Pergher, Mesoporous Materials for Reduction of Air Pollutants: Volatile Organic Compounds, Elsevier, Handbook of Nanomaterials for Industrial Applications, 2018, pp. 908–915.
[66] W.C. Conner, J.L. Falconer, Spillover in heterogeneous catalysis, Chemical reviews 95 (3) (1995) 759–788.